separations

Article

Numerical Simulation of Dense Solid-Liquid Mixing in Stirred Vessel with Improved Dual Axial Impeller

Xia Xiong [1,2], Zuohua Liu [1,2,*], Changyuan Tao [1,2], Yundong Wang [3] and Fangqin Cheng [4]

[1] School of Chemistry and Chemical Engineering, Chongqing University, Chongqing 400044, China; 20136395@cqu.edu.cn (X.X.); taocy@cqu.edu.cn (C.T.)
[2] State Key Laboratory of Coal Mine Disaster Dynamics and Control, Chongqing 400044, China
[3] Department of Chemical Engineering, Tsinghua University, Beijing 100084, China; wangyd@tsinghua.edu.cn
[4] Institute of Resources and Environment Engineering, Shanxi University, Taiyuan 030006, China; cfangqin@sxu.edu.cn
* Correspondence: liuzuohua@cqu.edu.cn

Abstract: Computational fluid dynamics (CFDs) were adopted in order to investigate the solid suspending process in a dense solid–liquid system (with a solid volume fraction of 30%), agitated by a traditional dual axial impeller and a modified dual axial impeller, otherwise known as a dual triple blade impeller (DTBI) and a dual rigid-flexible triple blade impeller (DRFTBI), respectively. The effects of rotational speed, connection strap length/width, and off-bottom clearance on the solid distribution were investigated. The results show that the proportion of solid concentration larger than 0.4 in the DTBI system was 26.56 times of that in the DRFTBI system. This indicates that the DRFTBI system can strengthen the solid suspension and decrease the solid accumulation in the bottom of the tank. Furthermore, the velocity and turbulent kinetic energy in the DRFTBI system were promoted. In addition, for an optimal selection, the optimum length of connection strap was 1.2 H_1, the optimum range of connection strap width was D/7–D/8, and the off-bottom clearance selected as T/4 was better.

Keywords: solid–liquid suspension; numerical simulation; high solid concentration; modified impeller

check for updates

Citation: Xiong, X.; Liu, Z.; Tao, C.; Wang, Y.; Cheng, F. Numerical Simulation of Dense Solid-Liquid Mixing in Stirred Vessel with Improved Dual Axial Impeller. *Separations* **2022**, *9*, 122. https://doi.org/10.3390/separations9050122

Academic Editor: Sohrab Zendehboudi

Received: 9 April 2022
Accepted: 10 May 2022
Published: 16 May 2022

Publisher's Note: MDPI stays neutral with regard to jurisdictional claims in published maps and institutional affiliations.

Copyright: © 2022 by the authors. Licensee MDPI, Basel, Switzerland. This article is an open access article distributed under the terms and conditions of the Creative Commons Attribution (CC BY) license (https://creativecommons.org/licenses/by/4.0/).

1. Introduction

Solid suspension in a stirred tank is a common operation in the process industry. It is common in the processes of hydrogenation, crystallization, leaching, precipitation, etc. [1]. In general, when the equipment requires a major upgrade, the production capacity of a plant is limited. Therefore, solid loading increasing could maximize the throughput or yield within the current production capacity. Moreover, it could improve the volume utilization rate of current tanks besides promoting the throughput. Thus, it has application value in the study of solid suspension in a stirred tank with high solid loading.

The accumulation of solid in the bottom of the tank is a common phenomenon in a high solid loading stirred tank, making it difficult to achieve good mixing effect. Drewer et al. [2] found that with increasing solid concentrations, a point was reached where suspension is unattainable. Tamburini et al. [3] found that with a solid concentration of 25% wsolid/wliquid, the sufficient suspension speed reaches up to 1100 rpm. This not only consumes high energy, but also places higher demands on the safety and stability of the equipment. Thus, studying the actions required to improve solid suspension in the high solid loading stirred tanks by process intensification is necessary.

Generally speaking, large stirring speed is a common way to improve solid suspension in stirred tanks. However, power consumption will increase sharply following an increase in rotation speed. There are some other methods available to strengthen mixing, such as eccentric stirring [4,5] and unsteady speed stirring [6]. These two methods are not conducive to the safe and stable operation of the equipment. There are some researchers who intensified the mixing process by improving the structure of the impeller. Xu et al. [7] found that the logarithmic helicoidal impeller could promote the solid suspension compared with rushton disc turbine impeller at the same power consumption. Zhao et al. [8] applied an improved Intermig impeller in the solid suspension process, and found that the improved Intermig impeller could promote the fluid circulation compared with the standard Intermig impeller. Gu et al. [9,10] designed a kind of rigid-flexible impeller and found that a longer and wider flexible connection piece is conducive to solid particles in suspension. Nevertheless, all of these methods were simply employed in concentration systems with low solidity. So far, only few efforts have been devoted to improving the solid suspension with a high solid loading. Thus, studies relevant to enhancing the high solid mixing system need to be carried out.

In order to observe the internal flow field, both experimental methods and numerical simulation methods could be adopted. Particle image velocimetry (PIV), laser doppler velocimetry (LDV), radioactive particle tracking (RPT), positron emission particle tracking (PEPT), and new invasive image velocimetry (NIIV) are some examples of experimental methods. Furthermore, the upper limit values of solid concentration that the fluid field can accurately measure are 8% [11], 15% [12], 7% [13], 10.4% [14], and 8.8% [15], respectively. Thus, the maximum value of the solid volume fraction which can be accurately measured by the fluid field is 15%. To sum up, there is still no suitable technique to measure the flow pattern of dense solid–liquid systems. One possible approach to predict suspension curves has been proposed by Tamburini et al. [16]. This model has reliable predictions starting from low impeller speed to complete suspension agitation speed. In addition, Tamburini et al. [17] predicted the minimum impeller speed for complete suspension in a dense solid–liquid suspension system using CFD simulation. Moreover, the concept of sufficient suspension was proposed to take the place of complete suspension. This suggests that the CFD method could effectively reveal the flow field of the dense solid–liquid suspension system. In summary, CFD simulation is more suitable than experimental studies for analyzing the flow field structure of the high solid loading system.

In this work, the CFD simulation was used to investigate the solid suspension in the dense solid concentration mixing system. Both the dual triple blade impeller (DTBI) and dual rigid-flexible triple blade impeller (DRFTBI) were used in this study. The effects of the impeller type, impeller speed, length and width of a connect piece, and off-bottom clearance on the solid–liquid mixing process were studied. The solid dispersion, the velocity profile, and the degree of uniformity were also analysed. The purpose was to explore an efficient impeller to strengthen solid suspension in a high solid loading mixing system.

2. System Studied

The mixing tank used in this study was a transparent flat-bottomed vessel with an inner diameter T = 0.18 m and a height H = 0.3 m. The height of liquid level H_L = 0.2 m. A sketch of the stirred tank is shown in Figure 1. The impellers used in this work include a dual triple blade impeller (DTBI) and a dual rigid-flexible triple blade impeller (DRFTBI), shown in Figure 2. The DRFTBI is the improvement of DTBI by connecting strap between two triple blade impellers. The slant angle of the blade is 45 degrees, the diameter of the impeller D = 0.07 m, and th e spacing of two impellers H_S = 0.1 m. The off-bottom clearance C is one of the investigated variables which can affect the suspension of solid. A dense solid–liquid suspension was studied: water and coal ash ($d_p \leq 75$ µm; $\rho = 2400$ kg/m^3) with the solid volume fraction equal to 30%. In order to comprehensively evaluate the mixing effect, different locations in the mixing tank were selected to analyse the result, as presented in Figure 3. The coordinate of vertical plane is X = 0; the coordinates of all horizontal planes are $Z_1 = 0\ H_L$, $Z_2 = 0.2\ H_L$, $Z_3 = 0.4\ H_L$, $Z_4 = 0.6\ H_L$, and $Z_5 = 0.8\ H_L$; and the coordinates of all the y lines are $y_1 = 2T/9$, $y_2 = 4T/9$, $y_3 = 6T/9$, and $y_4 = 8T/9$.

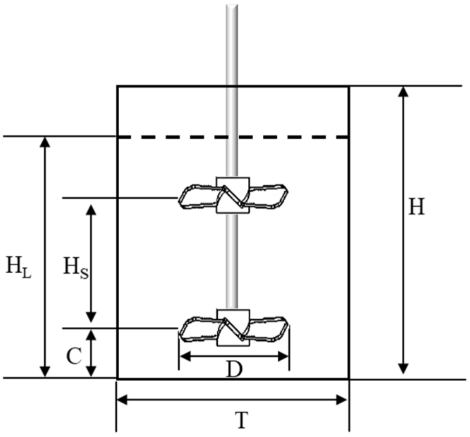

Figure 1. Sketch of the stirred tank.

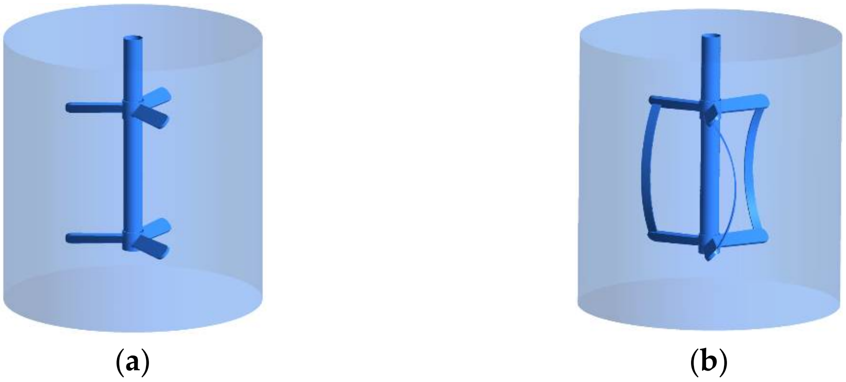

Figure 2. Structure of the impeller and the tank used in this work. (**a**) Dual triple blade impeller; (**b**) dual rigid-flexible triple blade impeller.

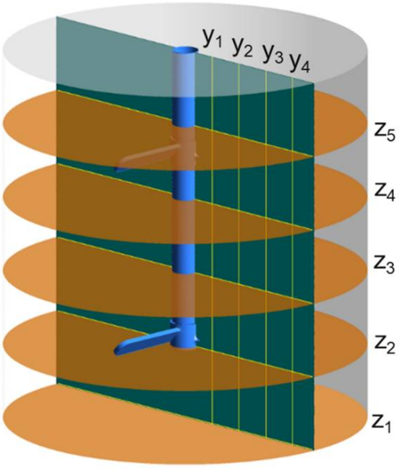

Figure 3. Distribution of the monitoring position in the vessel.

3. Computational Model and Details

The numerical solution of this 3D mixing system was implemented in the commercial CFD solver ANSYS Fluent 15.0. The Eulerian–Eulerian multi-fluid model was adopted for the simulation of a two-phase system. The continuity and momentum equations were solved separately and simultaneously. The coupling between the two phases was obtained via inter-phase exchange terms. All the details of the model equations have been listed as following:

3.1. Equations of Motion

The continuity equations [16]:

$$\frac{\partial}{\partial t}(\alpha_l\rho_l) + \vec{\nabla}\left(\alpha_l\rho_l\vec{U}_l\right) = 0 \tag{1}$$

$$\frac{\partial}{\partial t}(\alpha_s\rho_s) + \vec{\nabla}\left(\alpha_s\rho_s\vec{U}_s\right) = 0 \tag{2}$$

where the subscripts *l* and *s* refer to the continuous and dispersed phases, respectively; α is the volumetric fraction; ρ is the density; and U is the mean velocity.

Clearly,

$$\alpha_l + \alpha_s = 1 \tag{3}$$

The momentum balance equations:

$$\begin{aligned}&\tfrac{\partial}{\partial(t)}\left(\alpha_l\rho_l\vec{U}_l\right) + \vec{\nabla}\cdot\left\{\alpha_l\left[\rho_l\vec{U}_l\vec{U}_l - (\mu_l+\mu_{tl})\left(\vec{\nabla}\vec{U}_l + \left(\vec{\nabla}\vec{U}_l\right)^T\right)\right]\right\}\\ &= \alpha_l\left(\rho_l\vec{g} - \vec{\nabla}P\right) + \vec{F}_{l,s}\end{aligned} \tag{4}$$

$$\begin{aligned}&\tfrac{\partial}{\partial(t)}\left(\alpha_s\rho_s\vec{U}_s\right) + \vec{\nabla}\cdot\left\{\alpha_s\left[\rho_s\vec{U}_s\vec{U}_s - (\mu_s+\mu_{ts})\left(\vec{\nabla}\vec{U}_s + \left(\vec{\nabla}\vec{U}_s\right)^T\right)\right]\right\}\\ &= \alpha_s\left(\rho_s\vec{g} - \vec{\nabla}P\right) + \vec{F}_{s,l}\end{aligned} \tag{5}$$

where g is the gravitational acceleration, μ is the viscosity, μ_t is the turbulent viscosity, P is the pressure (the continuous and dispersed phases are assumed to share the same pressure field), and F is the interphase momentum transfer term.

3.2. Turbulence Model

The standard k-ε turbulence model was used to simulate the dense solid–liquid suspensions system in light of the research of Tamburini et al. [16,17]. In addition, the results were verified to be reliable. Thus, the standard k-ε turbulence model was applied in this work. Then, the continuous and dispersed phases were assumed to share the same turbulent kinetic energy k and the same turbulent energy dissipation rate ε. The equations are given as follows [16,17]:

$$\begin{aligned}&\tfrac{\partial}{\partial t}(\alpha_l\rho_l k) + \vec{\nabla}\left[\alpha_l\rho_l\vec{U}_l k - \alpha_l\left(\mu_l + \tfrac{\mu_{tl}}{\sigma_k}\right)\vec{\nabla}k\right]\\ &= \alpha_l\left(\mu_{tl}\vec{\nabla}\vec{U}_l\left(\vec{\nabla}\vec{U}_l + \left(\vec{\nabla}\vec{U}_l\right)^T\right) - \rho_l\varepsilon\right)\end{aligned} \tag{6}$$

$$\begin{aligned}&\tfrac{\partial}{\partial t}(\alpha_l\rho_l\varepsilon) + \vec{\nabla}\left[\alpha_l\rho_l\vec{U}_l\varepsilon - \alpha_l\left(\mu_l + \tfrac{\mu_{tl}}{\sigma_\varepsilon}\right)\vec{\nabla}\varepsilon\right]\\ &= \alpha_l\left(C_1\tfrac{\varepsilon}{k}\mu_{tl}\vec{\nabla}\vec{U}_l\left(\vec{\nabla}\vec{U}_l + \left(\vec{\nabla}\vec{U}_l\right)^T\right) - C_2\rho_l\tfrac{\varepsilon^2}{k}\right)\end{aligned} \tag{7}$$

where

$$\mu_{tl} = \rho_l C_\mu\frac{k^2}{\varepsilon} \tag{8}$$

3.3. Interphase Drag Force and Drag Coefficient

Interactions between the two phases were simulated by inter-phase drag force terms within the momentum equations [16]:

$$\vec{F}_{D,s} = -\vec{F}_{D,l} = \left[\frac{3}{4}\frac{C_D}{d_p}\alpha_l\rho_s\left|\vec{U}_l - \vec{U}_s\right|\right]\left(\vec{U}_l - \vec{U}_s\right) \tag{9}$$

where C_D is the inter-phase drag coefficient and was estimated using the Gidaspow drag model for densely distributed solid particles [14,18]:

$$C_D = \begin{cases} \frac{24}{\alpha_l Re_s}\left[1 + 0.15(\alpha_l Re_s)^{0.687}\right], Re_s < 1000 \\ 0.44, Re_s > 1000 \end{cases} \tag{10}$$

3.4. Numerical Details

In this study, the multiple reference frame (MRF) approach was employed to simulate impeller rotation [19–21]. The stirred tank was divided into two parts: the inner part was the rotating zone while the outer part was the non-rotating domain. The optimum grid size was obtained when the change in velocity and solid concentration profiles was less than 5%. The number of cells used for DTBI and DRFTBI was 754,916 and 895,634, respectively.

In this work, the SIMPLEC algorithm was used for pressure velocity coupling along with the standard pressure interpolation scheme. The hybrid-upwind discretization scheme was employed for the convective terms. In the initial simulation condition, a solid uniform average concentration of 30% was taken in the computational domain. The time step used in the simulation was 0.01 s, and the relative residual was set as 10^{-5}, which is considered as the index of convergence.

4. Results and Discussions

4.1. Verification of Modelling

Simulated results of the specific power consumption P_v were compared with experimental data in Figure 4a to validate the CFD model. The specific power consumption is defined as the impeller power draw divided by the total volume of solid and liquid. The power consumption in the agitated system could be calculated according to the formula [22–26]:

$$P_{sum} = 2\pi N M_a \tag{11}$$

Thus, the specific power consumption is:

$$P_v = \frac{P_{sum}}{V} = \frac{2\pi N M_a}{V} \tag{12}$$

where P_{sum} is the impeller power draw (W); V is the total volume of solid and liquid (m^3); N is the impeller rotational speed in revolutions per second (rps); and M_a is the absolute torque that could be obtained by using the torque transducer, determined according to the following equation [27]:

$$M_a = M_m - M_r \tag{13}$$

where M_m is the torque measured by the experiments, and M_r represents the residual torque cause of the mechanical friction in the bearing, determined by operating the impeller without any liquid or solid in the tank. Figure 4a shows that when the rotational speed was equal to 2 rps and the solid volume fraction was equal to 30%, the power consumption per unit volume of the experiment and simulation was 22.21 W/m^3 and 20.68 W/m^3, respectively. The variation of experimental data and the simulation result was 6.9%. Figure 4b shows the solid distribution between the simulation and the experiment. The stratification of solid distribution on the DTBI system can be seen as obvious, both in the simulation and experimental results, while the DRFTBI system significantly improved.

To sum up, the simulated results show a good agreement with those of corresponding experiments; therefore, the simulated results were reliable.

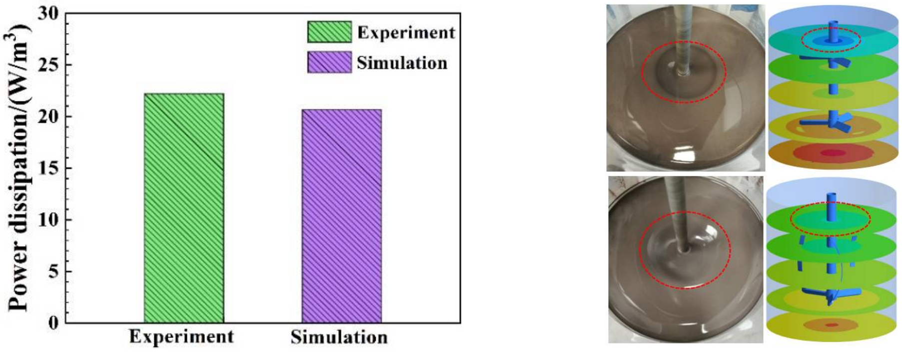

(**a**) (**b**)

Figure 4. (**a**) Comparation of P_v in the DRFTBI system between simulation and experiment; (**b**) comparation of solid distribution between the simulation and the experiment. (Rotational speed: 120 rpm; solid loading: 30%).

4.2. *Strengthening Effects of the Improved Impeller*

4.2.1. Comparison of Solid Particle Distribution

Figures 5 and 6 show the solid distribution of two kinds of stirred systems. It can be observed that the solid sedimentation on the bottom of a tank equipped with DRFTBI was less than a tank equipped with DTBI. Figure 7 shows the histogram of solid distribution for two mixing systems. The maximum value of the local solid concentration in the DTBI system was 0.58 and the maximum value of local solid concentration in the DRFTBI system was 0.49. The solid concentration proportions larger than 0.4 in the DRFTBI system and the DTBI system were 0.64% and 17%, respectively, which indicates that the DRFTBI could promote the solid suspension from the bottom. The solid concentration distribution of the DRFTBI system mainly aggregated in the range of 0.2–0.4 was close to the average concentration of 0.3, accounting for 94%. For the DTBI system, the proportion of solid concentration distribution below 0.2 and over 0.4 accounted for 39.8%, which was much larger than that in the DRFTBI system. This indicates that the DRFTBI could improve the uniform distribution. According to Figure 8, the dimensionless axial solid concentrations of the DRFTBI system at all Y lines were nearer to 1 compared to the DTBI system. This proves that the axial solid distribution was much more homogeneous in the DRFTBI tank.

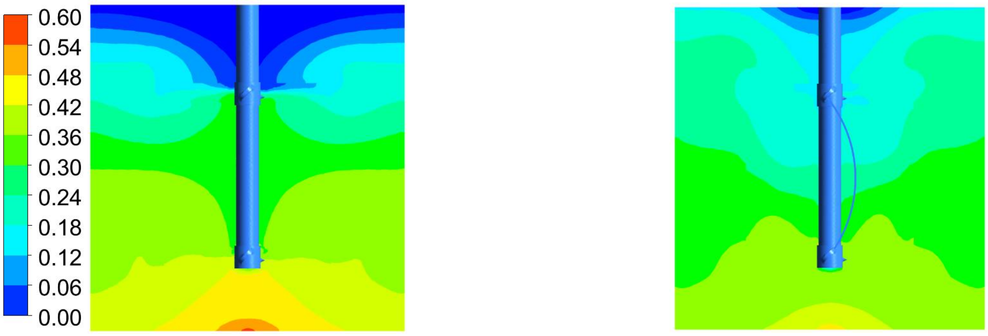

(**a**) (**b**)

Figure 5. Contour plots of solid distribution for different impeller types. (**a**) DTBI; (**b**) DRFTBI. (Rotational speed: 120 rpm; solid loading: 30%; connection strap length: 1.2 H_S; plane: X = 0).

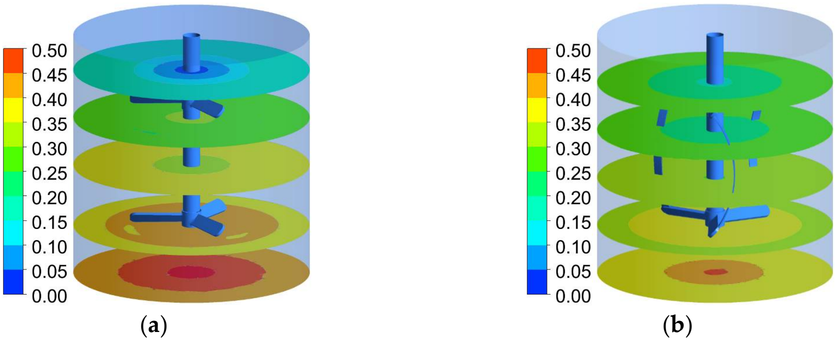

Figure 6. Contour plots of solid distribution for different impeller types. (**a**) DTBI; (**b**) DRFTBI. (Rotational speed: 120 rpm; solid loading: 30%; connection strap length: 1.2 H; plane: Z = 0 H, Z = 0.2 H, Z = 0.4 H, Z = 0.6 H, and Z = 0.8 H).

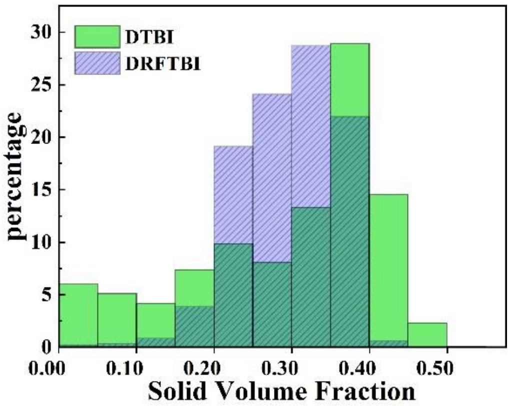

Figure 7. Histogram of solid distribution for different impeller types. (Rotational speed: 120 rpm; solid loading: 30%; connection strap length: 1.2 Hs).

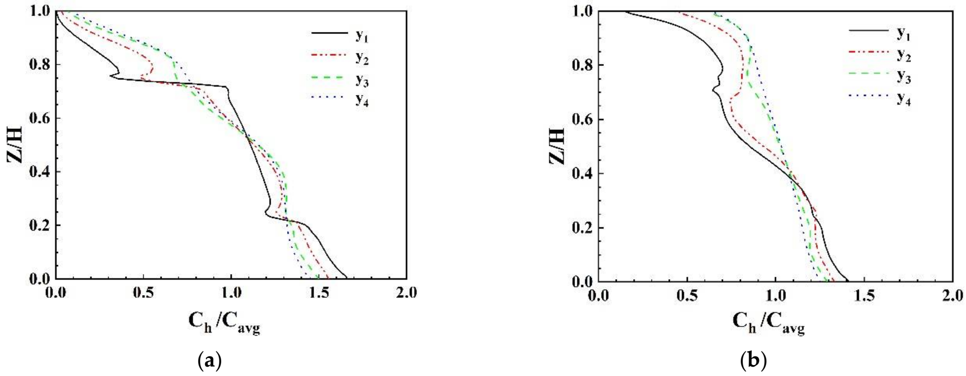

Figure 8. Axial solid concentration profile at different axial locations. (**a**) DTBI; (**b**) DRFTBI. (Rotational speed: 120 rpm; solid loading: 30%; connection strap length: 1.2 Hs).

4.2.2. Comparison of Velocity

Figure 9 shows the contour plots of velocity distribution for different impeller types. The value of velocity in the DRFTBI system was larger and the distribution of velocity was more uniform. The velocity profile at different axial locations was also demonstrated. According to Figure 10, the max dimensionless velocities of the DTBI system and the DRFTBI system were 0.26 and 0.36, respectively. The presence of the connecting belt increased the contact area of the fluid and the impeller, which can then drive more fluid and promote the whole fluid movement. Thus, the fluid velocity of the DRFTBI system was larger than that of the DTBI system. Moreover, in both two systems, the velocity in the regions close to the shaft or the wall was significantly lower than in the mid region; this is because the fluid flow was mainly influenced by the rotational motion of the impellers. Naturally, the fluid in the area close to the impeller could be more significantly influenced. Thus, in the near-shaft area, the flow velocity was smaller than the other areas.

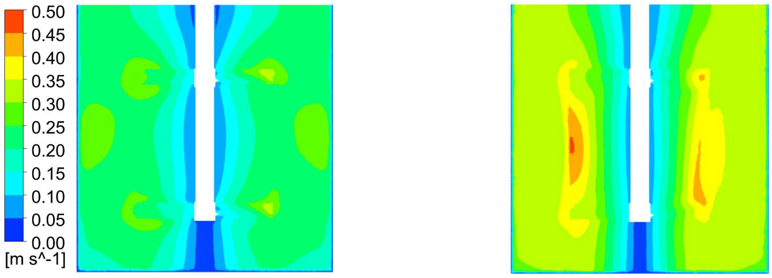

(**a**) (**b**)

Figure 9. Contour plots of velocity distribution for different impeller types. (**a**) DTBI; (**b**) DRFTBI. (Rotational speed: 120 rpm, Solid loading: 30%, Connection strap length: 1.2 H_S, Plane: X = 0).

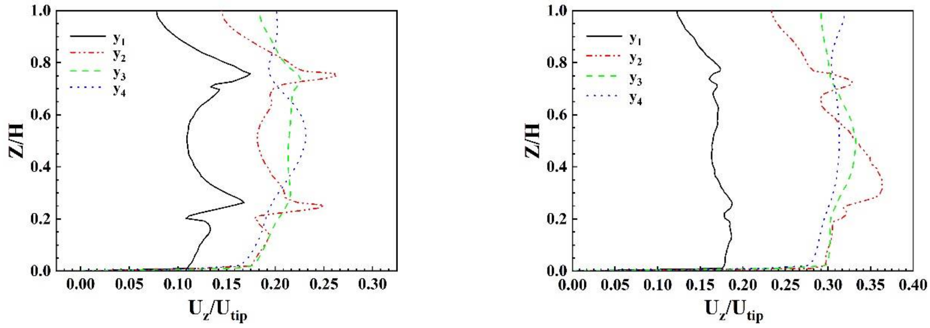

(**a**) (**b**)

Figure 10. Velocity profile at different axial location. (**a**) DTBI; (**b**) DRFTBI. (Rotational speed: 120 rpm; solid loading: 30%; connection strap length: 1.2 Hs).

4.2.3. Comparison of Turbulent Kinetic Energy

Figure 11 shows that the variation tendency of turbulent kinetic energy in the stirred tank was similar to the velocity. Turbulent kinetic energy in the regions close to the shaft or the wall was lower in the mid region. A comparation of turbulent kinetic energies at each axial location is shown in Figure 12. At the location of y_1 and y_2, the difference of turbulent kinetic energy profile between two systems was not so significant. However, at the location of y_3 and y_4, turbulent kinetic energy for the DRFTBI system was larger than that for the DTBI system. This is because the connecting belt expanding the zone of the impeller can affect the tank, promoting fluid turbulence. The results show that the DRFTBI could strengthen the turbulent kinetic energy in the region close to wall.

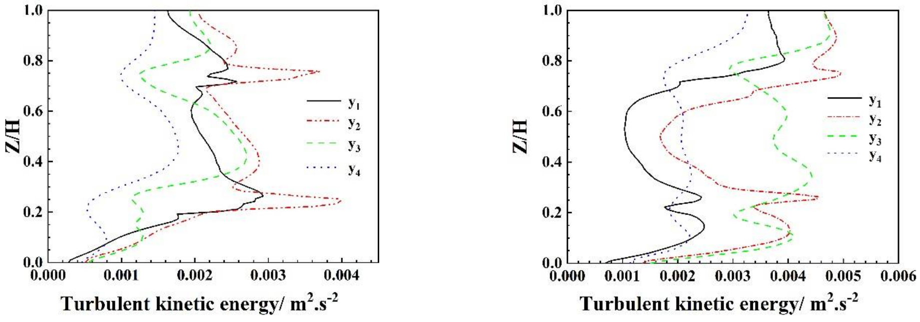

(**a**) (**b**)

Figure 11. Turbulent kinetic energy profile at different axial location. (**a**) DTBI; (**b**) DRFTBI. (Rotational speed: 120 rpm; solid loading: 30%; connection strap length: 1.2 Hs).

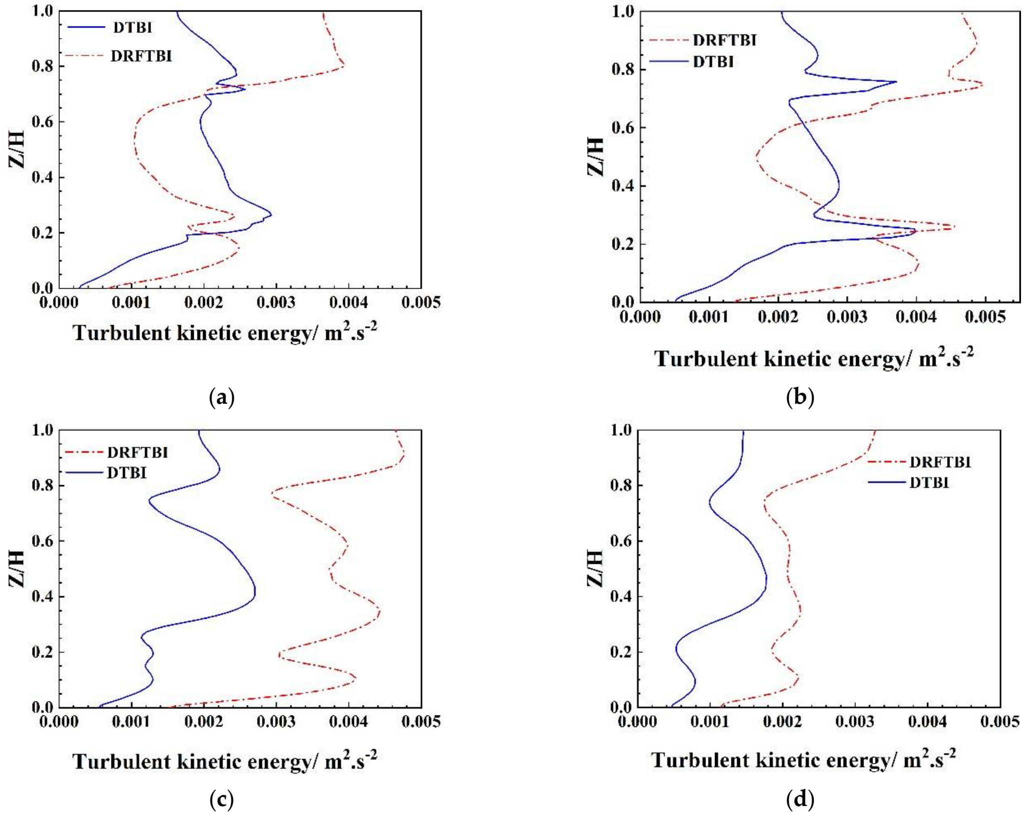

(**a**) (**b**)

(**c**) (**d**)

Figure 12. Comparation of turbulent kinetic energy profiles between two systems. (**a**) y_1; (**b**) y_2; (**c**) y_3; (**d**) y_4. (Rotational speed: 120 rpm; solid loading: 30%; connection strap length: 1.2 Hs).

4.2.4. Comparison of Homogeneity

The homogeneity ξ is a parameter which is often used to evaluate the solid suspension quality in the stirred tank. It can be calculated as [17]:

$$\xi = 1 - \sqrt{\frac{1}{n}\sum_{n=1}^{n}\left(\frac{C_h}{C_{avg}} - 1\right)^2} \tag{14}$$

Figure 13 illustrates the axial ξ as a function of the radial position for DTBI and DRFTBI. As displayed in Figure 13, in both the DTBI system and the DRFTBI system, the axial ξ will increase following an increase in the distance away from the shaft. In addition, the value of axial ξ in the DRFTBI system was always larger than that in the DTBI system; thus, the DRFTBI system could strongly promote the solid suspension quality. Meanwhile, according to Figure 14, the deviation of axial ξ between the two systems was not very large. This indicates that the strengthening effect of the DRFTBI system was in the global range of the stirred tank, not just a local region.

The mechanism of the strengthening effect of DRFTBI is shown in Figure 15. The strengthening process is carried out in two main steps. The first step is the solid suspension. The cavity formation, broken in the first stage of stirring, can induce many vortexes. These vortexes can promote solid suspension by enhancing the fluctuation of fluid flowing. The second step is the solid particle distribution. After solid particles are in suspension, they can crash with the connection strap or flow with the fluid driven by the connection strap. Furthermore, the solid particle could be distributed in bulk of the stirred tank during this process.

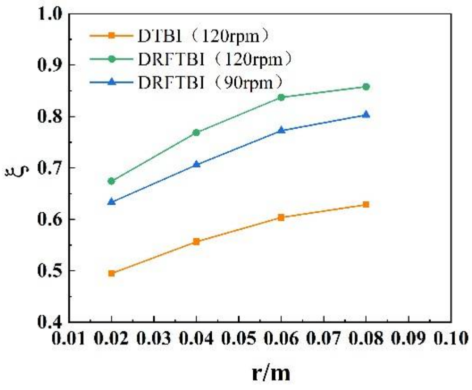

Figure 13. Comparation of homogeneity in the two systems. (Solid loading: 30%; connection strap length: 1.2 Hs).

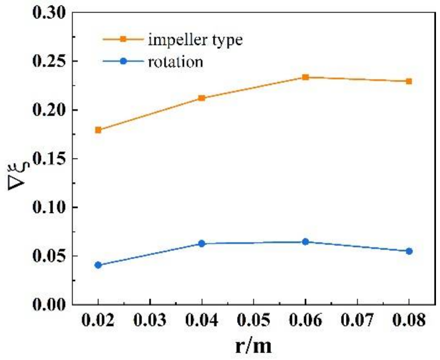

Figure 14. Deviation of axial ξ at different axial locations. (Solid loading: 30%; connection strap length: 1.2 Hs).

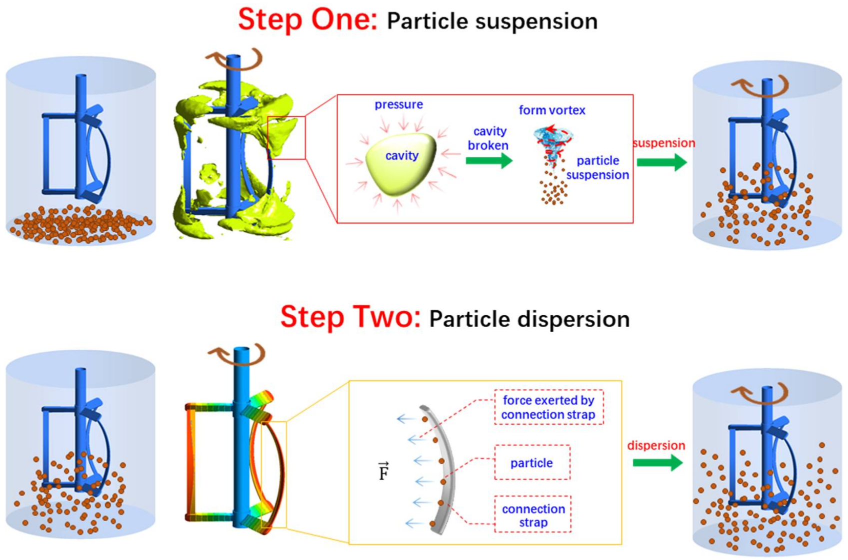

Figure 15. The schematic diagram of DRFTBI strengthens the solid suspension.

4.3. Effect of Rotation Speed

Solid distribution under different rotational speed has been studied and the results are shown in Figure 16. As expected, the solid aggregation at the bottom of tank decreased following an increase in rotational speed. The solid distribution was quantified, as shown in Figure 17. When the rotational speed increased from 90 rpm to 120 rpm, the proportion of solid concentration larger than 0.4 decreased from 3.9% to 0.6%, and the proportion of solid concentration in the range of 0.25–0.35 increased from 49.5% to 52.9%. The results indicate that increasing the rotational speed could slightly improve the suspension and distribution of solid.

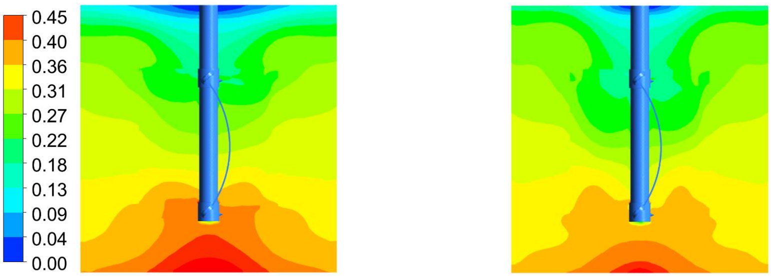

(**a**) (**b**)

Figure 16. Contour plots of solid distribution for DRFTBI at different rotational speeds. (**a**) 90 rpm; (**b**) 120 rpm. (Rotational speed: 120 rpm; solid loading: 30%; connection strap length: 1.2 Hs; plane: X = 0).

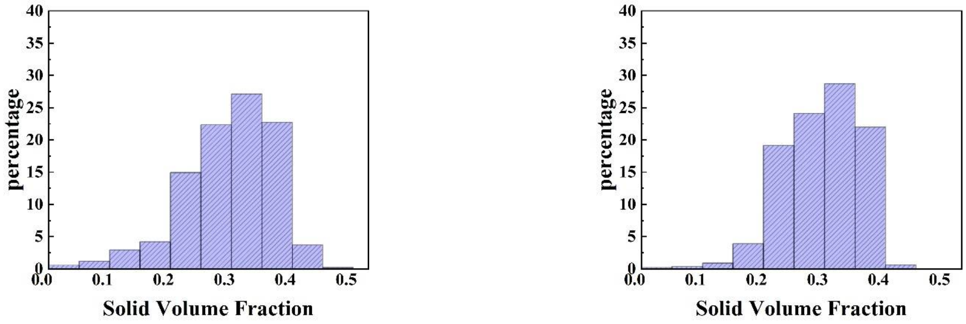

(**a**) (**b**)

Figure 17. Histogram of solid distribution for DRFTBI at different rotational speeds. (**a**) 90 rpm; (**b**) 120 rpm. (Rotational speed: 120 rpm; solid loading: 30%; connection strap length: 1.2 Hs).

4.4. Effect of Connection Strap Length

The results of the solid distribution for DRFTBI with different connection strap lengths are shown in Figure 18. Furthermore, the histograms of solid distribution are shown in Figure 19. To discover the effect of connection strap length on solid distribution, the proportion of solid concentration in the range of 0.25–0.35 and larger than 0.35 is discussed. The proportions in the range of 0.25–0.35 for a connection strap length of 1.1 Hs, 1.2 Hs, and 1.3 Hs were 45.6%, 52.9%, and 52.6%, respectively. Furthermore, the proportions in the range larger than 0.35 for connection strap lengths of 1.1 Hs, 1.2 Hs, and 1.3 Hs were 26.7%, 22.6%, and 22.6%, respectively. The results show that the better connection strap, as opposed to the longer one, was intensified by increasing the connection strap within a certain range of length.

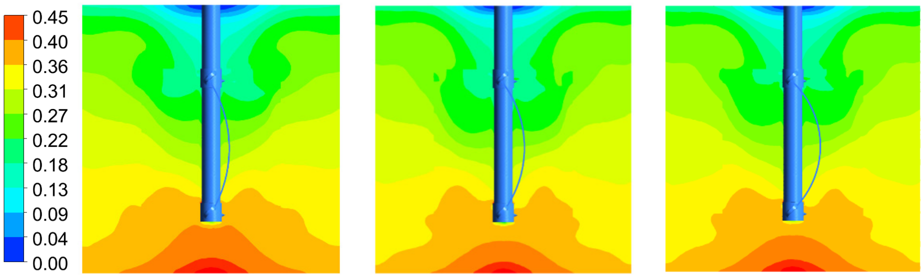

(**a**) (**b**) (**c**)

Figure 18. Contour plots of solid distribution for DRFTBI with different connection strap lengths. (**a**) 1.1 Hs; (**b**) 1.2 Hs; (**c**) 1.3 Hs. (Rotational speed: 120 rpm; solid loading: 30%; plane: X = 0).

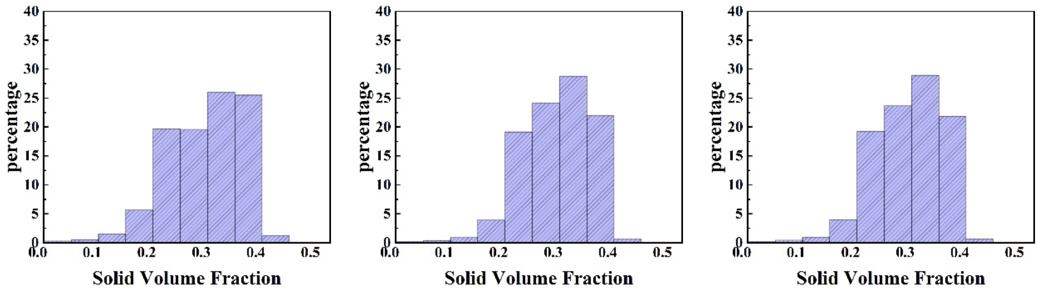

(**a**) (**b**) (**c**)

Figure 19. Histogram of solid distribution for DRFTBI with different connection strap length. (**a**) 1.1 Hs; (**b**) 1.2 Hs; (**c**) 1.3 Hs. (Rotational speed: 120 rpm; solid loading: 30%).

4.5. Effect of Connection Strap Width

The results of solid distribution for DRFTBI with different connection strap widths are shown in Figure 20. Furthermore, the histograms of solid distribution are shown in Figure 21. According to Figure 20, the proportions in the range larger than 0.35 for connection strap widths of D/5, D/6, D/7, D/8, and D/9 were 16.5%, 25.3%, 22.6%, 24.1%, and 25.5%, respectively. Except for D/5 and D/9, the accumulation of solid in the bottom of the tank had no significant difference between the other strap width investigated in this study, as the maximum difference among them is lower than 3%. The wider the connection strap, the greater the resistance. For D/5, the strap was wider than the others; thus, the power consumption must be higher than others. Thus, from the perspective of power consumption, D/5 was not the best choice of strap width. However, for a narrow connection strap, although the resistance was lower, the solid accumulation rate was relatively high. So, D/9 was also not the best choice of strap width. To maintain the balance of power consumption and the mixing effect, a better option for a connection strap width should be the range of D/8–D/7.

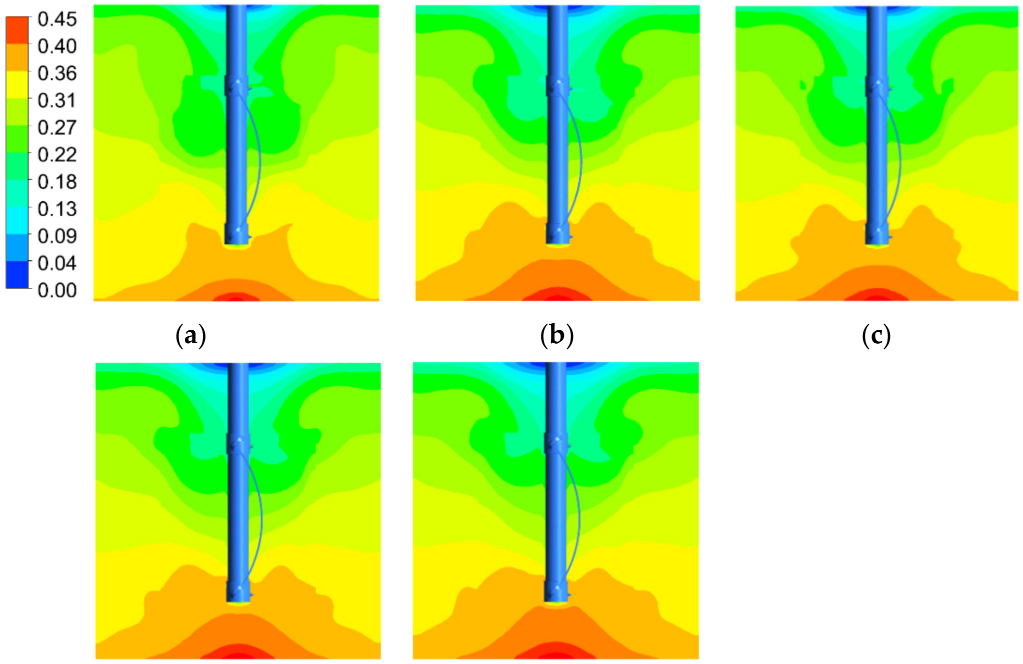

(**a**) (**b**) (**c**)

(**d**) (**e**)

Figure 20. Contour plots of solid distribution for DRFTBI with different connection strap width. (**a**) D/5; (**b**) D/6; (**c**) D/7; (**d**) D/8; and (**e**) D/9. (Rotational speed: 120 rpm; solid loading: 30%; connection strap length: 1.2 Hs).

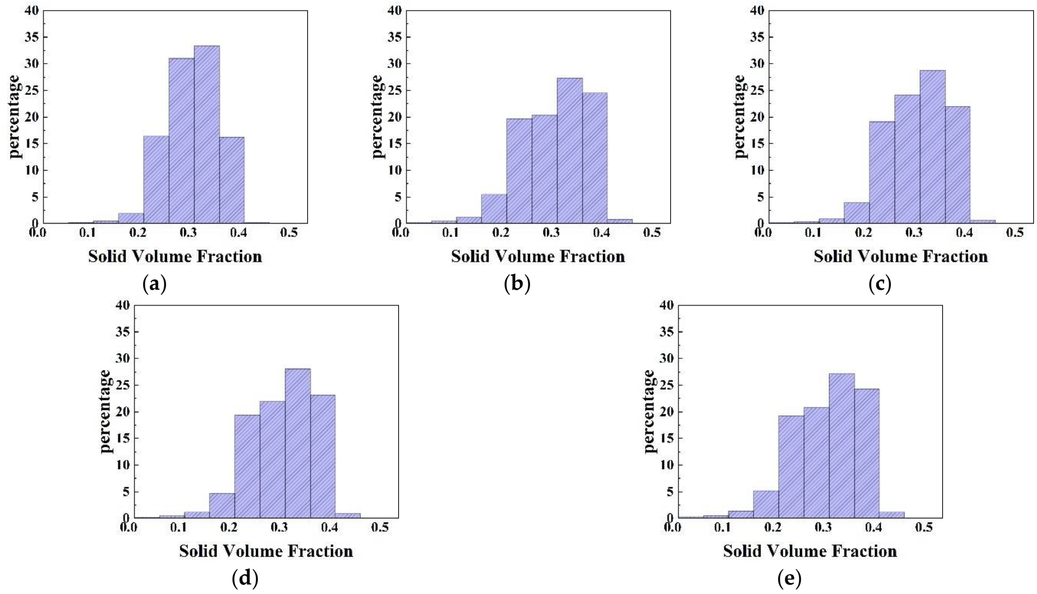

(**a**) (**b**) (**c**) (**d**) (**e**)

Figure 21. Histogram of solid distribution for DRFTBI with different connection strap widths. (**a**) D/5; (**b**) D/6; (**c**) D/7; (**d**) D/8; and (**e**) D/9. (Rotational speed: 120 rpm; solid loading: 30%; connection strap length: 1.2 Hs).

4.6. Effect of Off-Bottom Clearance

The results of solid distribution for DRFTBI with different off-bottom clearances are shown in Figure 22. Furthermore, the histograms of solid distribution are shown in Figure 23. With the increase in off-bottom clearance, the accumulation of solid in the bottom of tank decreased, and the distribution of solid in the upper part of the tank improved. When the off-bottom clearance increased from T/5 to T/3, the proportions of solid concentration larger than 0.4 were 23.1%, 0.65%, and 0.96%, respectively, while the proportions of solid concentration lower than 0.2 were 22.9%, 16.38%, and 14.03%, respectively. For the low solid loading system, when the impeller was close to the bottom, the mixing effect and driving force for solid suspension in the lower part of the tank was relatively better than in the upper part. Unlike the low solid loading system, a mass of solid weight on the blades of the impeller in the high loading system weakened the solid suspension effect and resulted in an accumulation of solid in the bottom of the tank.

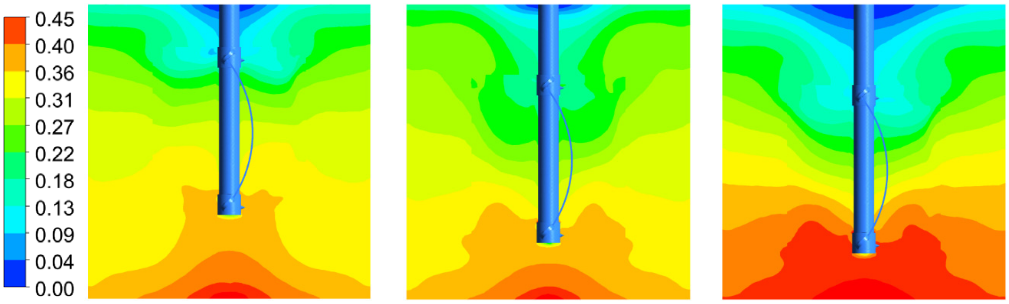

(**a**) (**b**) (**c**)

Figure 22. Contour plots of solid distribution for DRFTBI with different off-bottom clearance. (**a**) T/3; (**b**) T/4; and (**c**) T/5. (Rotational speed: 120 rpm; solid loading: 30%; connection strap length: 1.2 Hs).

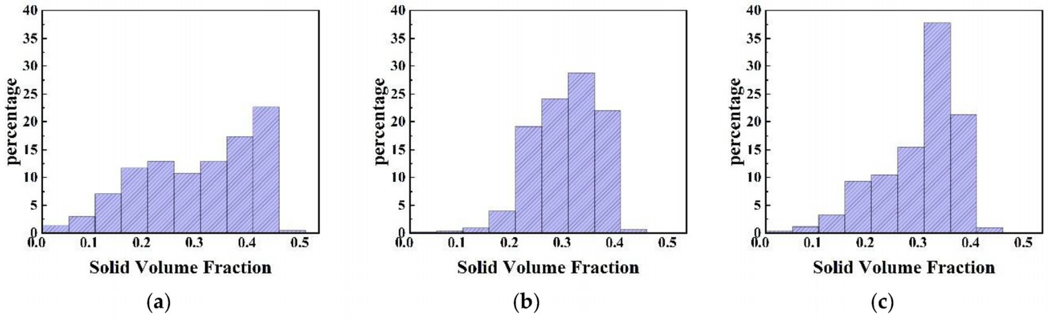

(**a**) (**b**) (**c**)

Figure 23. Histogram of solid distribution for DRFTBI with different off-bottom clearance. (**a**) T/3; (**b**) T/4; and (**c**) T/5. (Rotational speed: 120 rpm; solid loading: 30%; connection strap length: 1.2 Hs).

5. Conclusions

This paper studies the intensification of solid suspension and homogeneous distribution in a high solid loading mixing system using the CFD method. The DTBI and DRFTBI systems were investigated. The simulated results showed that DRFTBI had better mixing performance compared to DTBI. Meanwhile, the effects of impeller speed, connection strap length/width, and off-bottom clearance were investigated. The main conclusions are listed below.

(1) The local solid concentration of the DRFTBI system was lower than that of the DTBI system. Meanwhile, the proportion of solid concentration in the range of 0.25–0.3 was increased, meaning that more region with a solid concentration closer to the average concentration. In conclusion, the DRFTBI system could promote the suspension of solid in the stirred tank and enhance the homogeneity. This is because the DRFTBI could induce many vortexes in order to enhance the solid suspension. On the other hand, solid particle crash with a connection strap could their distribution in bulk of the stirred tank.

(2) Longer strap lengths were not the best. The strengthening effect of increasing the strap length only worked in a definite range. For the strap width, the promotion of particle suspension was limited when the strap was too thin. Thus, the strap width was most effective in the range of D/7–D/8, whereby variation was only small between each width.

(3) For the off-bottom clearance, when the initial solid concentration was the same, a lower impeller location could accumulate more solid in the impeller blades, thus inhibiting the rotation of the impeller. Thus, the lower off-bottom clearance did not improve the mixing in the lower part of the tank, as expected.

Author Contributions: Conceptualization, Z.L., Y.W. and F.C.; methodology, X.X., Z.L., Y.W. and C.T.; investigation, X.X.; resources, Z.L. and C.T.; Supervision, Z.L., Y.W. and C.T.; writing—original draft preparation, X.X. and Z.L.; writing—review and editing, X.X. and Z.L.; supervision, Z.L.; funding acquisition, Z.L. and Y.W. All authors have read and agreed to the published version of the manuscript.

Funding: The study was supported by the National Natural Science Foundation of China (22078030, Z20200804), National Key Research and Development Project (2019YFC1905802), Key Project of Independent Research Project of State Key Laboratory of Coal Mine Disaster Dynamics and Control (2011D-A105287-zd201902), Hubei Three Gorges Laboratory Open/Innovation Fund (SK211009, SK215001).

Institutional Review Board Statement: Not applicable.

Informed Consent Statement: Not applicable.

Data Availability Statement: The data presented in this study are available on request from the corresponding author.

Conflicts of Interest: The authors declare no conflict of interest.

Nomenclature

C	off-bottom clearance (m)
C_h	local solid volume fraction at height of h
C_{avg}	average solid volume fraction
$C_{\varepsilon 1}, C_{\varepsilon 2}, C_{\varepsilon 3}, C_{\mu}$	ὺparameters in the standard k-ε model
C_D	drag coefficient
D	impeller diameter (m)
d_p	particle diameter (m)
F	interphase momentum transfer term (N)
F_{drag}	drag force (N)
g	gravitational acceleration (m/s^2)
H	stirred vessel height (m)
H_L	liquid height (m)
H_S	interlayer spacing of two impeller (m)
k	turbulent kinetic energy (m^2/s^2)
M_a	absolute torque (N.m)
M_m	torque measured experimentally (N.m)
M_r	residual torque (N.m)
N	impeller speed (rpm)
n	number of sampling points
P	pressure (Pa)
P_{sum}	power consumption (W)
P_v	specific power consumption (W/m^3)
r	radial coordinate (m)
T	inner diameter of stirred vessel (m)
t	time (s)
U_i	velocity (m/s)
V	total volume of solid and liquid (m^3)
Greek Letters	
ρ_l	liquid density (kg/m^3)
ρ_s	solid density (kg/m^3)
ρ	density (kg/m^3)
α	volume fraction
α_l	liquid phase volume fraction
α_s	solid phase volume fraction
ε	turbulent energy dissipation rate
μ	viscosity ($Pa \cdot s$)
μ_l	liquid phase viscosity ($Pa \cdot s$)
μ_t	turbulent viscosity ($Pa \cdot s$)
μ_{tl}	liquid phase turbulent viscosity ($Pa \cdot s$)
σ_k , σ_ε	k and ε turbulent Prandtl number
ξ	homogeneity

References

1. Carletti, C.; Montante, G.; Westerlund, T.; Paglianti, A. Analysis of solid concentration distribution in dense solid–liquid stirred tanks by electrical resistance tomography. *Chem. Eng. Sci.* **2014**, *119*, 53–64. [CrossRef]
2. Drewer, G.R.; Ahmed, N.; Jameson, G.J. Suspension of High Concentration Solids in Mechanically Stirred Vessels. In *Institution of Chemical Engineers Symposium Series*; Hemisphere Publishing Corporation: London, UK, 1994; Volume 136, p. 41.
3. Tamburini, A.; Cipollina, A.; Micale, G.; Brucato, A.; Ciofalo, M. CFD simulations of dense solid–liquid suspensions in baffled stirred tanks: Prediction of solid particle distribution. *Chem. Eng. J.* **2013**, *223*, 875–890. [CrossRef]
4. Woziwodzki, S.; Jędrzejczak, A. Effect of eccentricity on laminar mixing in vessel stirred by double turbine impellers. *Chem. Eng. Res. Des.* **2011**, *89*, 2268–2278. [CrossRef]
5. Zhang, M.; Hu, Y.; Wang, W.; Shao, T.; Cheng, Y. Intensification of viscous fluid mixing in eccentric stirred tank systems. *Chem. Eng. Processing Process Intensif.* **2013**, *66*, 36–43. [CrossRef]
6. Nomura, T.; Uchida, T.; Takahashi, K. Enhancement of Mixing by Unsteady Agitation of an Impeller in an Agitated Vessel. *J. Chem. Eng. Jpn.* **1997**, *30*, 875–879. [CrossRef]

7. Lin, R.; Stuckman, M.; Howard, B.H.; Bank, T.L.; Roth, E.A.; Macala, M.K.; Lopano, C.; Soong, Y.; Granite, E.J. Application of sequential extraction and hydrothermal treatment for characterization and enrichment of rare earth elements from coal fly ash. *Fuel* **2018**, *232*, 124–133. [CrossRef]
8. Zhao, H.L.; Zhang, Z.M.; Zhang, T.A.; Yan, L.I.U.; Gu, S.Q.; Zhang, C. Experimental and CFD studies of solid-liquid slurry tank stirred with an improved Intermig impeller. *Oral Oncol.* **2014**, *50*, 2650–2659. [CrossRef]
9. Gu, D.; Liu, Z.; Xie, Z.; Li, J.; Tao, C.; Wang, Y. Numerical simulation of solid-liquid suspension in a stirred tank with a dual punched rigid-flexible impeller. *Adv. Powder Technol.* **2017**, *28*, 2723–2734. [CrossRef]
10. Gu, D.; Liu, Z.; Qiu, F.; Li, J.; Tao, C.; Wang, Y. Design of impeller blades for efficient homogeneity of solid-liquid suspension in a stirred tank reactor. *Adv. Powder Technol.* **2017**, *28*, 2514–2523. [CrossRef]
11. Li, G.; Gao, Z.; Li, Z.; Wang, J.; Derksen, J.J. Particle-resolved PIV experiments of solid-liquid mixing in a turbulent stirred tank. *AIChE J.* **2018**, *64*, 389–402. [CrossRef]
12. Kohnen, C.; Bohnet, M. Measurement and Simulation of Fluid Flow in Agitated Solid/Liquid Suspensions. *Chem. Eng. Technol.* **2001**, *24*, 639–643. [CrossRef]
13. Guha, D.; Ramachandran, P.A.; Dudukovic, M.P. Flow field of suspended solids in a stirred tank reactor by Lagrangian tracking. *Chem. Eng. Sci.* **2007**, *62*, 6143–6154. [CrossRef]
14. Liu, L.; Barigou, M. Numerical modelling of velocity field and phase distribution in dense monodisperse solid–liquid suspensions under different regimes of agitation: CFD and PEPT experiments. *Chem. Eng. Sci.* **2013**, *101*, 837–850. [CrossRef]
15. Wang, H.; Li, X.; Mao, Z.S.; Yang, C. New invasive image velocimetry applicable to dense multiphase flows and its application in solid–liquid suspensions. *AIChE J.* **2019**, *65*, e16668. [CrossRef]
16. Tamburini, A.; Cipollina, A.; Micale, G.; Brucato, A.; Ciofalo, M. CFD simulations of dense solid–liquid suspensions in baffled stirred tanks: Prediction of suspension curves. *Chem. Eng. J.* **2011**, *178*, 324–341. [CrossRef]
17. Tamburini, A.; Cipollina, A.; Micale, G.; Brucato, A.; Ciofalo, M. CFD simulations of dense solid–liquid suspensions in baffled stirred tanks: Prediction of the minimum impeller speed for complete suspension. *Chem. Eng. J.* **2012**, *193*, 234–255. [CrossRef]
18. Li, X.K. *Multiphase Flow and Fluidization, Continuum and Kinetic Theory Descriptions*; Gidaspow, D., Ed.; Academic Press: New York, NY, USA, 1993; p. 467, Price $60.00; ISBN 0-12-282770-9. *J. Non-Newton. Fluid Mech.* **1994**, *55*, 207–208.
19. Klenov, O.P.; Noskov, A.S. Solid dispersion in the slurry reactor with multiple impellers. *Chem. Eng. J.* **2011**, *176*, 75–82. [CrossRef]
20. Hosseini, S.; Patel, D.; Ein-Mozaffari, F.; Mehrvar, M. Study of Solid−Liquid Mixing in Agitated Tanks through Computational Fluid Dynamics Modeling. *Ind. Eng. Chem. Res.* **2010**, *49*, 4426–4435. [CrossRef]
21. Qi, N.; Zhang, H.; Zhang, K.; Xu, G.; Yang, Y. CFD simulation of particle suspension in a stirred tank. *Particuology* **2013**, *11*, 317–326. [CrossRef]
22. Hashemi, N.; Ein-Mozaffari, F.; Upreti, S.R.; Hwang, D.K. Analysis of mixing in an aerated reactor equipped with the coaxial mixer through electrical resistance tomography and response surface method. *Chem. Eng. Res. Des.* **2016**, *109*, 734–752. [CrossRef]
23. Hashemi, N.; Ein-Mozaffari, F.; Upreti, S.R.; Hwang, D.K. Analysis of power consumption and gas holdup distribution for an aerated reactor equipped with a coaxial mixer: Novel correlations for the gas flow number and gassed power. *Chem. Eng. Sci.* **2016**, *151*, 25–35. [CrossRef]
24. Jegatheeswaran, S.; Kazemzadeh, A.; Ein-Mozaffari, F. Enhanced aeration efficiency in non-Newtonian fluids using coaxial mixers: High-solidity ratio central impeller with an anchor. *Chem. Eng. J.* **2019**, *378*, 122081. [CrossRef]
25. Hashemi, N.; Ein-Mozaffari, F.; Upreti, S.R.; Hwang, D.K. Experimental investigation of the bubble behavior in an aerated coaxial mixing vessel through electrical resistance tomography (ERT). *Chem. Eng. J.* **2016**, *289*, 402–412. [CrossRef]
26. Jegatheeswaran, S.; Ein-Mozaffari, F. Investigation of the detrimental effect of the rotational speed on gas holdup in non-Newtonian fluids with Scaba-anchor coaxial mixer: A paradigm shift in gas-liquid mixing. *Chem. Eng. J.* **2020**, *383*, 123118. [CrossRef]
27. Wang, S.; Parthasarathy, R.; Wu, J.; Slatter, P. Optimum Solids Concentration in an Agitated Vessel. *Ind. Eng. Chem. Res.* **2014**, *53*, 3959–3973. [CrossRef]